



Characterization and Testing of Additively Manufactured Porous Ceramic Electro spray Emitters

Luke D'Cruz*, Carl Geiger†, Suhail Chamieh‡, Ben Inbar §, Sadaf Sobhani¶, and Elaine Petro||
Cornell University, Ithaca, NY, 14850

Additively manufactured porous ceramic electro spray emitters developed with microscale 3-D printing have shown potential to operate similarly to electro spray emitters fabricated via subtractive manufacturing methods. However, the emission behavior of additively manufactured emitters requires further characterization. In this work, we develop a porous ceramic emitter via two-photon polymerization and characterize its emission performance with 1-Ethyl-3-methylimidazolium tetrafluoroborate (EMI-BF₄) using direct current-applied voltage measurements and time-of-flight mass spectrometry. 3-D geometrical characterization of the emitters is performed via scanning electron microscope and laser scanning confocal microscope imaging.

I. Introduction

AN electro spray thruster is an electric propulsion system that operates by extracting ions from an ionic liquid propellant to form a Taylor cone and accelerating these ions through an applied electric field. An electro spray thruster is composed of thousands of single electro spray emitters. A porous emitter is a conically-shaped microstructure that utilizes capillary action to passively draw propellant to the base of the Taylor cone. Electro spray emitters boast precision thrust control and very high specific impulse, making them ideal for satellite on-orbit precise attitude control [1] or primary propulsion for micro-satellites.

Many of the electro spray emitters produced by industry and academia are fabricated using subtractive manufacturing methods, such as electrochemically etched tungsten [2], deep reactive ion etching [3], and laser ablated porous silica [4]. With the advent of two-photon polymerization (TPP) printers, it is possible to achieve the microscale resolution necessary for additively manufacturing electro spray emitters. TPP is a non-linear process that uses a femtosecond pulsed laser to polymerize resin within the voxel of the laser, enabling the creation of 3D features smaller than the diffraction limit of the laser beam [5].

Previous characterization of the porous alumina emitter performance has shown that these emitters can produce stable emission, with direct current recorded as a function of applied voltage (I-V measurements) between the emitter and a grounded extractor plate [6]. To characterize the emitter's ion plume along with its thrust and specific impulse, time-of-flight mass spectrometry (TOF-MS) is performed alongside emitted current measurements. By measuring the time it takes for the charged particles from the emitter plume to travel a known flight distance, the mass-to-charge ratio of these species can be determined. Thrust can be inferred by accounting for the emitted current [7].

II. Methods

This section presents the general approach undertaken for this work, detailing the procedures that were utilized to create and characterize the emitter. The emitter was fabricated using additive manufacturing processes and then structurally analyzed using surface science techniques. Finally, the emitter was fired under vacuum, and its emission was characterized via plume diagnostic methods.

*Ph.D. Student, Mechanical and Aerospace Engineering, Cornell University, AIAA Student Member

†Ph.D. Student, Mechanical and Aerospace Engineering, Cornell University, AIAA Student Member

‡Graduate Student, Mechanical and Aerospace Engineering, Cornell University, AIAA Student Member

§Research Assistant, Mechanical and Aerospace Engineering, Cornell University, AIAA Student Member

¶Assistant Professor, Mechanical and Aerospace Engineering, Cornell University, AIAA Member

||Assistant Professor, Mechanical and Aerospace Engineering, Cornell University, AIAA Member

A. Emitter Fabrication

This emitter fabrication process builds upon the procedure presented by S. Chamieh et al. [6]. A mold of the emitter tip is printed with IP-Q resin using a Nanoscribe GT2 TPP printer with a 10x objective lens. This mold is printed onto a UV-cured resin substrate made with an Elegoo Mars 2 Pro stereolithography printer. The substrate-mold sample is bathed in 1-methoxy-2-propanol acetate (PGMEA) for 3 hours to remove excess IP-Q resin and then soaked in isopropyl alcohol (IPA) for 30 minutes to remove the PGMEA. The sample is dried with compressed air and placed in a 405 nm curing station for 2 minutes.

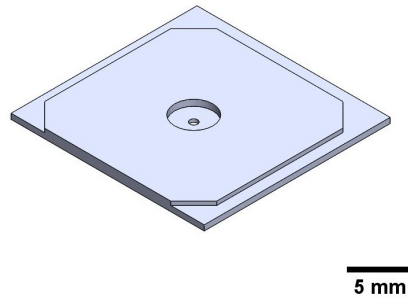


Fig. 1 Isometric view of resin substrate CAD model.

The substrate contains a circular cutout which acts as the mold for the emitter base. The substrate surface in contact with the emitter mold contains a through hole (Fig. 1), which allows for the filling of the base and tip molds as one continuous volume. After the emitter tip mold is printed and cured, a 30G hypodermic needle is used to fill the emitter tip mold with commercial alumina slurry (AdmaPrint A130). The sample is placed in a dessicator to remove air trapped in the slurry and then is exposed to UV light to cure the slurry. Consecutive slurry layers are applied, with vacuum and UV-curing steps repeated for each layer of slurry.

Once completely filled, the substrate-mold sample is placed in a Nabertherm muffle furnace to burn off the substrate, mold tip, and ceramic binder matrix. The furnace heats up to 600°C at a rate of 600°C/hr and holds at this temperature for 2 hours. Once the sample is passively cooled to room temperature, it is placed in a Nabertherm sintering furnace to partially sinter the emitter, following a modified version of Admatec's commercial alumina sintering program guidelines. The sintering temperature peaks at 1400°C, a modification which allows the emitter maintain its desired porosity [6]. A general overview of the fabrication process is shown in Fig. 2. Once the emitter has been sintered, its external geometry and surface finish can be characterized with a scanning electron microscope (SEM) and a laser confocal microscope (LCM).



Fig. 2 Overview of the emitter fabrication process.

B. Emitter Geometry Characterization

1. Scanning Electron Microscope Imaging

A Zeiss LEO 1550 scanning electron microscope provided high-resolution images of the emitter, enabling emitter surface analysis post-sintering and general visualization of the emitter's external geometry. The emitter shown in Fig. 3 was sintered at a maximum temperature of 1400°C, with dwell times matching Admatec commercial guidelines.

The SEM image of the emitter surface was analyzed with ImageJ to estimate emitter porosity. The image underwent contrast adjustments and thresholding in order to identify and count the individual bright grains and dark pores.

Assuming a circular pore area, the average pore size r_p was estimated by calculating total pore area and averaging over the number of pores to find the average radius. Average grain size r_g was calculated in a similar manner, but a watershed algorithm was used to further isolate the grains during image processing. Based on the average pore and grain radii and assuming spherical pores and grains, the emitter porosity ϕ was then determined by dividing the pore volume by the combined pore and grain volume. The emitter permeability κ was calculated using the Kozeny-Carman equation (Eq. 1), assuming spherical grains.

$$\kappa = \frac{\phi^3(2r_g)^2}{180(1-\phi)^2} \quad (1)$$

Average emitter pore size for this work was found to be 0.087 μm , with a standard deviation of 0.022 μm . Average grain size was found to be 0.23 μm , with a standard deviation of 0.13 μm . The emitter porosity was calculated to be 5.21%, and estimated permeability was $1.85 \times 10^{-19} \text{ m}^2$.

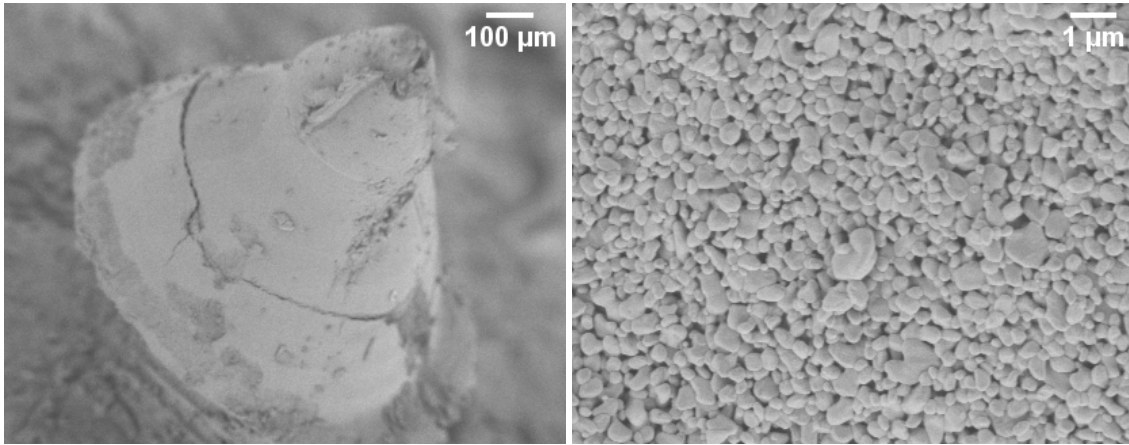


Fig. 3 SEM images of a sintered porous alumina emitter.

2. Laser Scanning Confocal Microscope Imaging

A Keyence VK-X260 laser scanning confocal microscope was also used to image emitters. A laser scanning confocal microscope (LSCM) offers a non-intrusive, nanometer-resolution method of imaging emitters at atmosphere, while also requiring less sample preparation than SEM imaging. The LSCM also possesses the ability to produce a 3-D render of a sample when given a 2-D view of the sample (i.e. imaging the top of the sample). This is useful for visualizing the external geometry and surface finish of emitter tips. Because the laser can only accurately scan flat or convex surface features, additional LSCM or SEM imaging at a 45° angle is necessary to more precisely characterize the emitter's surface. However, the LSCM provides a rapid and convenient method for imaging emitters prior to using more labor intensive methods. Additionally, the LSCM's laser profilometer feature has the ability to produce a surface profile of the emitter, which can be used to determine the emitter's height, angle, and radius of curvature. Figure 4 shows LSCM images of a porous alumina emitter.

Figure 5 depicts the surface cross-sectional profile of the emitter. The surface profile shows that the emitter has a height of 1.6 mm. ImageJ analysis of the emitter surface profile indicates that the emitter has a half-angle of 33.0° and a radius of curvature of 59.6 μm . The LSCM images and surface profile suggest the presence of defects and undesired surface roughness on the emitter's tip. We hypothesize that these features develop due to interactions between the alumina slurry and emitter mold during the debind phase of the fabrication process. Future efforts will require materials analysis of the slurry, paying particular attention to its debinding behavior.

C. Experimental Setup

The ceramic emitter is held onto a stainless steel SEM stub with conducting carbon tape, and the stub is securely fit into a 1"x 1"x 1" PTFE block using a set screw that doubles as the high voltage connection point. A micropipette is used

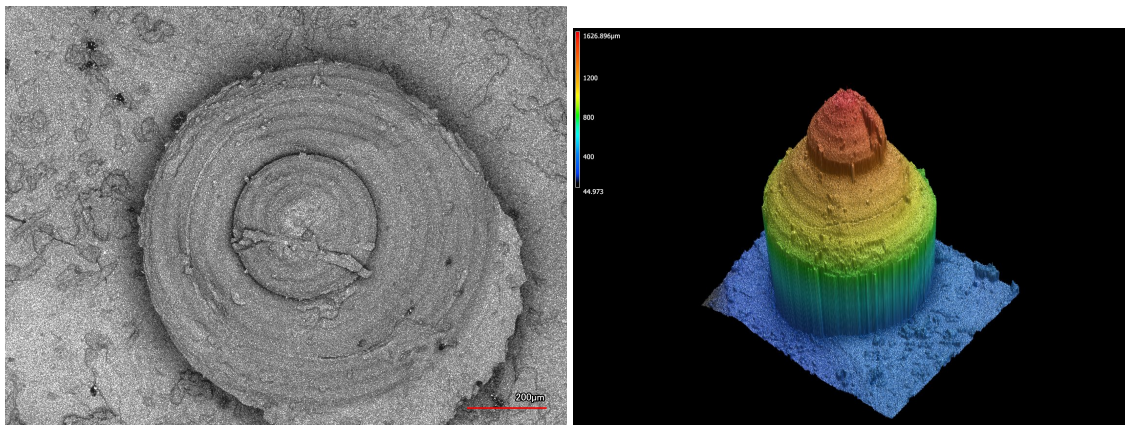


Fig. 4 LSCM images of a sintered porous alumina emitter.

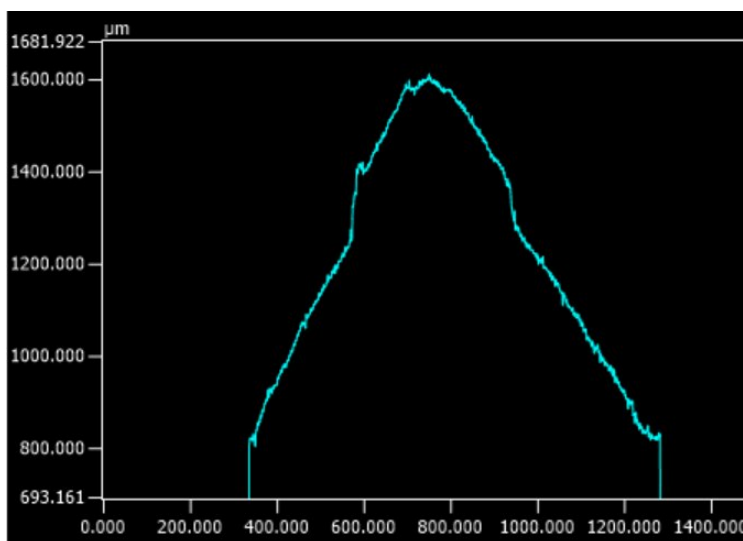


Fig. 5 Surface profile of emitter cross-section.

to drop approximately $0.5 \mu\text{L}$ of EMI-BF_4 onto the emitter tip which absorbs into the porous structure. The PTFE block is mounted to a larger assembly, shown in Fig. 6, which includes a precision 3 axis linear stage for aligning the extractor electrode, a goniometer for controlling the pitch angle of the ion source, and a rotational stage for controlling the yaw angle. Tests were performed inside a $\varnothing 24'' \times 20''$ cylindrical vacuum chamber operated by a rotary vane backing pump and a turbo molecular pump. The background pressure for all testing was around 10^{-5} Torr.

III. Results

A. I-V Curve

Figure 7 shows the emitted current at an applied voltage between ± 3 kV. The current intercepted by the extractor electrode could not be recorded due to equipment failure. The onset potential required to fire was $+2.56$ and -2.62 kV for the positive and negative mode, respectively.

After the onset firing voltage is reached in the positive mode, the emitted current increases approximately linearly by voltage, at a rate of roughly $16.2 \frac{\mu\text{A}}{\text{V}}$ with a maximum at 3 kV of $7.2 \mu\text{A}$, while in the negative mode the emitted current increases by roughly $14.7 \frac{\mu\text{A}}{\text{V}}$ with a maximum at -3 kV of $-5.8 \mu\text{A}$. These are high currents for single electro spray

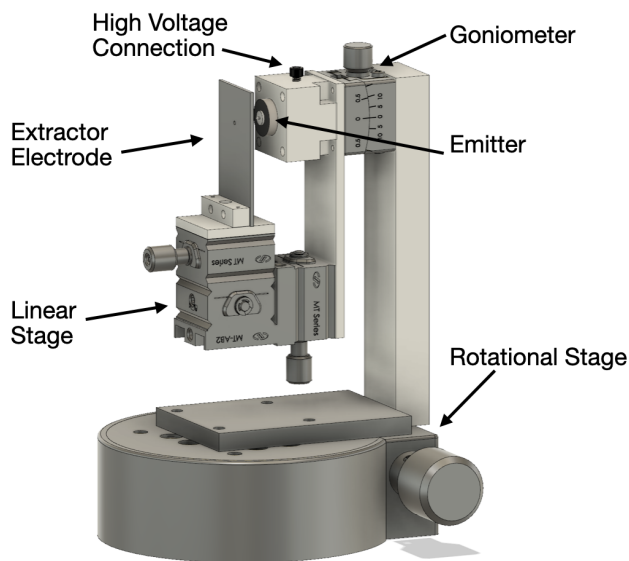


Fig. 6 Ceramic emitter electro spray source configuration.

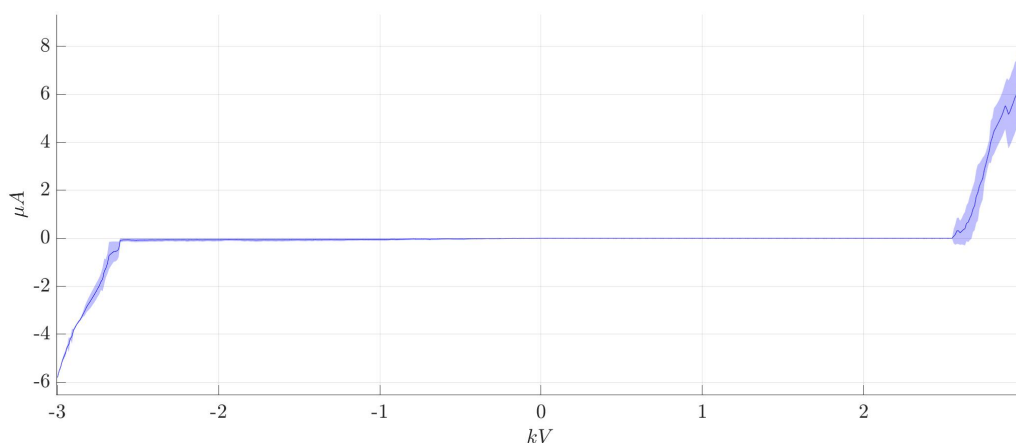


Fig. 7 Emitted current as a function of applied voltage. Shaded area represents one standard deviation.

emitters operating in the ion mode, which may indicate multiple emission sites forming, possibly on defects found near the emitter tip.

Figure 8 shows the firing region of the I-V curve expanded, along with firing data captured with a previous ceramic emitter from an earlier effort by S. Chamieh et al. [6]. The onset voltage for the previous emitter was +2.3 kV and -2.3 kV with a current increase of roughly $0.13 \frac{\mu A}{V}$ in the positive mode with a maximum of 90 nA and $0.05 \frac{\mu A}{V}$ in the negative mode with a maximum of -35 nA.

B. Time-of-Flight Measurements

The time-of-flight spectrum was collected in the positive and negative mode using a flight tube about 1 meter long with a microchannel plate (MCP) at the end coupled with a transimpedance amplifier. The ion gate consists of two parallel electrodes connected to a high voltage power supply and controlled with a 20 MHz Keysight waveform generator. Mass is reported assuming all species are singly charged and data are smoothed using a 3rd order Savitzky–Golay filter. Figure 9 shows the time of flight curve in the positive mode, indicating emission of primarily monomers (EMI^+) and dimers ($[EMI^+][EMI-BF_4]$), as well as an anomalous mass at 286 Da which is thought to be contamination, though the species and source is unknown.

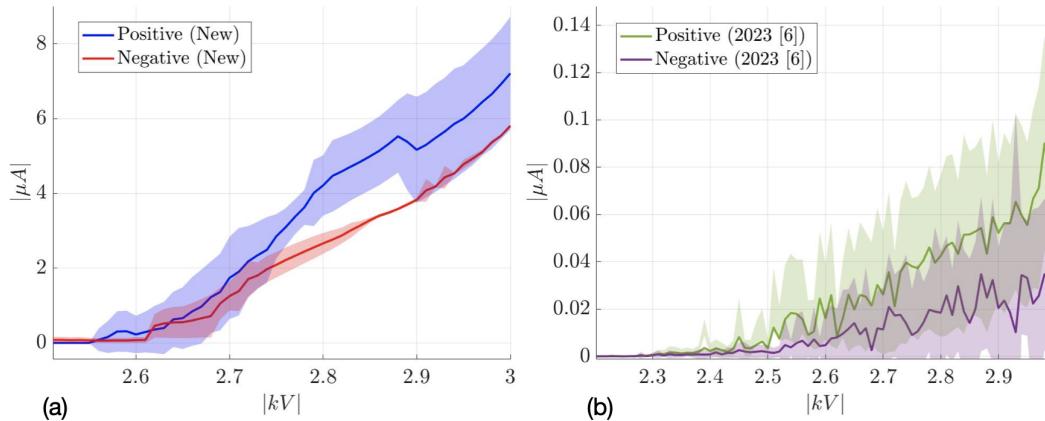


Fig. 8 Expanded firing region of I-V curve plotted as absolute emitted current as a function of absolute applied voltage: a) newest ceramic emitter, b) ceramic emitter from S. Chamieh et al. [6]. Shaded area represents one standard deviation.

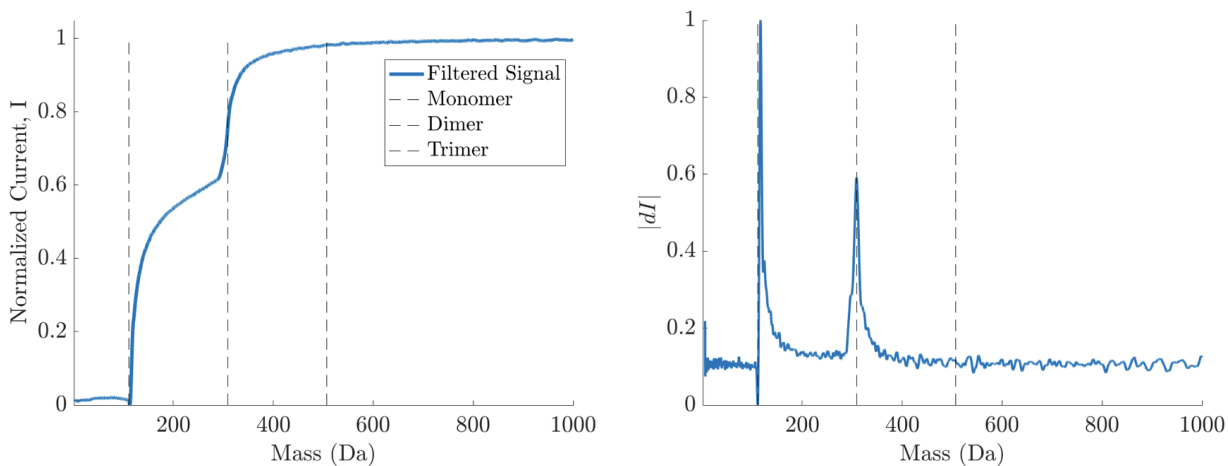


Fig. 9 Time of flight data for positive ion mode electrospray source. Mass of monomer, dimer, and trimer species are included.

In order to drive the electrons generated in the MCP channels toward the output, a -1 kV potential is applied to the outer most plate; this makes collecting mass spectra of negative ions only possible when the ions have sufficient energy to overcome the -1 kV potential, and still enough energy to induce secondary electron emission at the MCP. The positive and negative ion plumes were fired at ± 2.8 kV, which is sufficient for negative ion mass spectra collection. Figure 10 shows the time of flight curve in the negative mode, with a relatively larger monomer (BF_4^-) population and only a sparse dimer ($[\text{BF}_4^-][\text{EMI-BF}_4]$) population.

Figure 11 shows the time-of-flight data for an extended collection period, allowing for the detection of much larger species. Here the anomalous mass at 286 Da is seen again and more prevalent. After the trimer species line, a gradual decrease in current is seen, indicating a population of more massive droplets mixed with the ion plume. It does not appear the curve levels to zero completely within the window sampled, and so it is possible that even larger droplets are present.

1. Performance Estimates

From the time-of-flight results, estimates of the thrust and mass flow rate of the centerline of the plume can be calculated using Eqs. 2 and 3 respectively [8]:

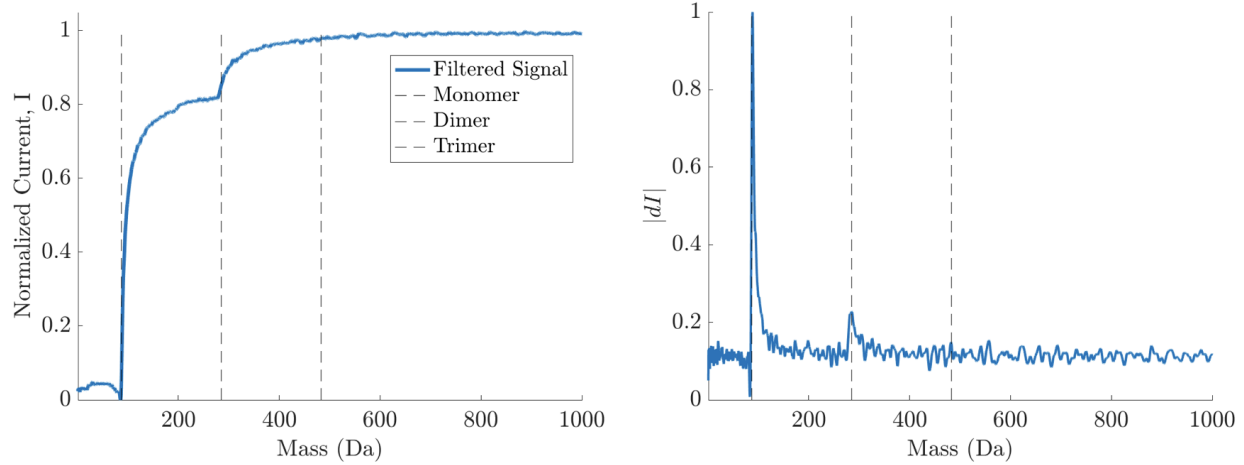


Fig. 10 Time of flight data for negative ion mode electrospray source. Mass of monomer, dimer, and trimer species are included.

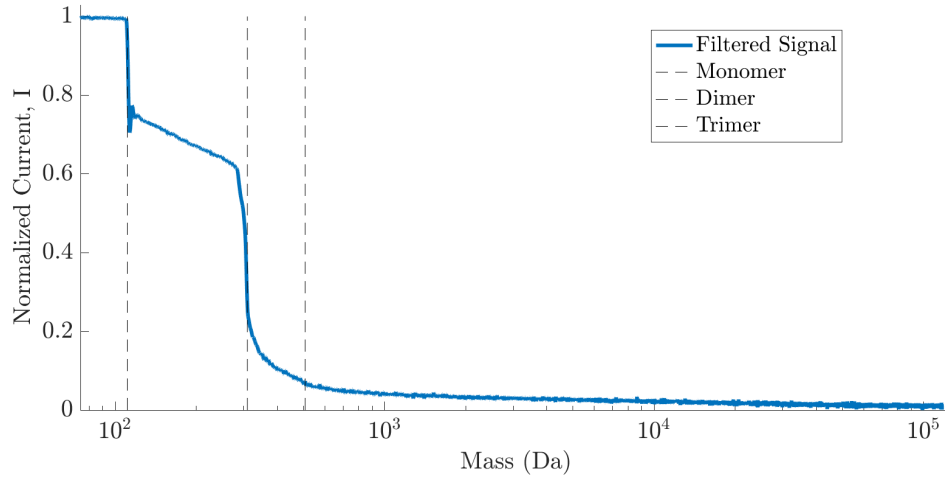


Fig. 11 Extended time of flight data for positive ion mode electrospray source, plotted on a log scale. Mass of monomer, dimer, and trimer species are included.

$$T = \frac{-2V_0 I_b}{L_{tof}} \int_0^{t_{max}} t \frac{d\bar{I}}{dt} dt \quad (2)$$

$$\dot{m} = \frac{-2V_0 I_b}{L_{tof}^2} \int_0^{t_{max}} t^2 \frac{d\bar{I}}{dt} dt \quad (3)$$

where V_0 is the firing potential, I_b is the total beam current, L_{tof} , and \bar{I} is the beam current fraction. The estimated specific impulse can be found using Eq. 4:

$$I_{sp} = \frac{T}{g\dot{m}} \quad (4)$$

where g is the acceleration due to gravity on Earth. Using the time-of-flight results in 11, the specific impulse of the centerline of the plume was estimated to be 1950 s. This estimate does not account for neutral fragmentation products and as previously stated, there may be a heavy droplet population not captured by the time-of-flight data, and so the true specific impulse will be lower.

2. Multi-Charged Droplets

Larger droplets can hold multiple charges, so long as the coulombic repulsion of the charges cannot overcome the droplet surface tension. A charged droplet is at the Rayleigh limit when these competing forces are balanced [9]. The net charge of a droplet at the Rayleigh limit can be calculated using:

$$Q_r = 8\pi(\epsilon_0\gamma R^3)^{1/2} \quad (5)$$

where ϵ_0 is the permittivity of the vacuum and γ is the surface tension of the droplet. Figure 12 shows the high mass end of the time-of-flight curve, shaded to represent the possible charge state of the droplets.

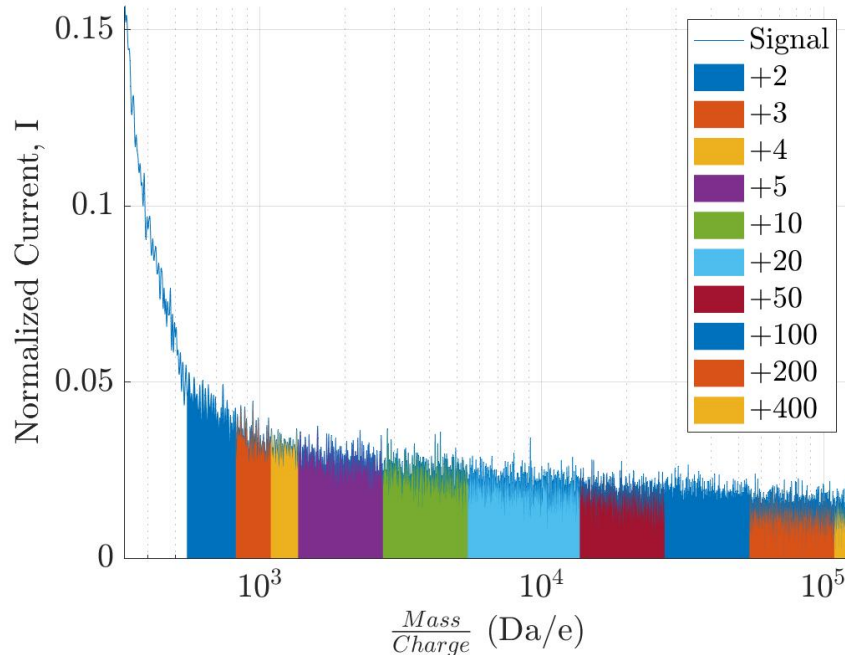


Fig. 12 High mass end of the time-of-flight curve, shaded regions represent possible charge state of the droplets.

In the time-of-flight window sampled in this study it is possible droplets with a charge state of nearly +500 appear in the spectrum, though this would imply an exceptionally high mass flow rate, depleting the ionic liquid in a fraction of the total firing time observed, and therefore droplets holding a high number of elementary charges likely do not represent a significant portion of the plume.

IV. Conclusion

This work expands upon our previous fabrication process for additively manufacturing porous ceramic electrospay emitters using two-photon polymerization. This publication also describes an additional emitter surface analysis method for characterizing the emitter geometry. Emitter firing is characterized using standard plume diagnostic methods. The findings from this effort suggest that further experimentation with single emitters is necessary to eliminate surface defects and better understand their emission characteristics.

Future Work

Future work will include further characterization of the emitter plume using retarding potential analysis and beam divergence measurements. The internal development and optimization of ceramic slurries will be performed in order to produce on-demand quantities of emitters of consistent quality. Additionally, material interactions between the substrate, mold, and slurry during the debind process will be investigated to optimize emitter geometry and finish. Finally, future research efforts will explore the capability of existing facilities to produce multiple emitters in the form of an array.

Acknowledgments

The authors thank Zachary Ulibarri and Stefan Bell for fruitful discussions regarding this work and their help collecting TOF data. The authors also acknowledge experimental support from Diya Mehta and Emily Harmon. This work was supported by the Science, Mathematics, and Research for Transformation (SMART) Scholarship, funded by the Office of the Undersecretary of Defense for Research & Engineering (OUSD/R&E), National Defense Education Program (NDEP). This work was supported by a NASA Space Technology Graduate Research Opportunity. The authors acknowledge the use of facilities and instrumentation supported by NSF through the Cornell University Materials Research Science and Engineering Center DMR-1719875. This work was performed in part at the Cornell NanoScale Facility, a member of the National Nanotechnology Coordinated Infrastructure (NNCI), which is supported by the National Science Foundation (Grant NNCI-2025233).

References

- [1] Ziemer, J., Marrese-Reading, C., Dunn, C., Romero-Wolf, A., Cutler, C., Javidnia, S., Li, T., Li, I., Franklin, G., and Barela, P., “Colloid microthruster flight performance results from space technology 7 disturbance reduction system.” *The 35th International Electric Propulsion Conference*, 2017.
- [2] Lozano, P., and Martinez-Sanchez, M., “Ionic liquid ion sources: characterization of externally wetted emitters,” *Journal of Colloid and Interface Science*, Vol. 282, No. 2, 2005, pp. 415–421. <https://doi.org/10.1016/j.jcis.2004.08.132>.
- [3] Velasquez-Garcia, L. F., Akinwande, A. I., and Martinez-Sanchez, M., “A micro-fabricated linear array of electrospray emitters for thruster applications,” *Journal of Microelectromechanical Systems*, Vol. 15, No. 5, 2006, pp. 1260–1271. <https://doi.org/10.1109/jmems.2006.879707>.
- [4] MacArthur, J. V., “Material and fabrication developments in the ion-electrospray propulsion system,” Ph.D. thesis, Massachusetts Institute of Technology, 2020.
- [5] Maruo, S., Nakamura, O., and Kawata, S., “Three-dimensional microfabrication with two-photon-absorbed photopolymerization,” *Optics Letters*, Vol. 22, No. 2, 1997, pp. 132–134. <https://doi.org/10.1364/ol.22.000132>.
- [6] Chamieh, S., Petro, E., and Sobhani, S., “Additive Manufacturing and Characterization of Porous Ceramic Electrospray Emitters,” *AIAA SCITECH 2023 Forum*, 2023, p. 0261.
- [7] Lyne, C. T., Liu, M. F., and Rovey, J. L., “A Low-Cost Linear Time-of-Flight Mass Spectrometer for Electrospray Propulsion Diagnostics,” *The 37th International Electric Propulsion Conference*, 2022.
- [8] Gamero-Castano, M., and Hruby, V., “Electrospray as a Source of Nanoparticles for Efficient Colloid Thrusters,” *Journal of Propulsion and Power*, Vol. 17, No. 5, 2001, pp. 977–987. <https://doi.org/10.2514/2.5858>.
- [9] Konermann, L., “A Simple Model for the Disintegration of Highly Charged Solvent Droplets during Electrospray Ionization,” *Journal of the American Society for Mass Spectrometry*, Vol. 20, No. 3, 2009, pp. 496–506. <https://doi.org/https://doi.org/10.1016/j.jasms.2008.11.007>, URL <https://www.sciencedirect.com/science/article/pii/S1044030508009896>.